Extreme rejuvenation of a bulk metallic glass at the nanoscale by swift heavy ion irradiation

S. Khademorezaian [a],[*], M. Tomut [a],[b], M. Peterlechner [a],[c], M.W. da Silva Pinto [a], H. Rösner [a], S. Divinski [a], G. Wilde [a]

[a] *Institute of Materials Physics, University of Münster, Wilhelm-Klemm-Str. 10, 48149 Münster, Germany*
[b] *Materials Research Department, Gesellschaft für Schwerionenforschung (GSI), Darmstadt, Germany*
[c] *Laboratory for Electron Microscopy, Karlsruhe Institute for Technology, Engesserstr. 7, Karlsruhe 76131, Germany*

A R T I C L E   I N F O

A B S T R A C T

Swift heavy ions can be used as a tool to tune material properties by generating high aspect ratio, nanometric trails of defects, or new disordered phases. This work explores different aspects of using this tool for rejuvenating and enhancing plasticity in bulk metallic glasses. An amorphous alloy with a nominal composition of $Pd_{40}Ni_{40}P_{20}$ was irradiated with GeV-accelerated Au ions. Irradiation-induced out-of-plane swelling steps up to approximately 100 nm in height are measured at the boundary between irradiated and non-irradiated areas. Changes of the relaxation enthalpy have been investigated using differential scanning calorimetry. Low-temperature heat capacity measurements substantiate an irradiation-induced increase of the boson peak height with increasing fluences. Accompanying transport measurements using radioactive Ag atoms as tracer also revealed increased diffusion rates in the irradiated samples dependent on the total fluence. Nano-indentation measurements show enhanced plasticity in the ion-irradiated glass which can be correlated with an increased heterogeneity as indicated by variable resolution fluctuation electron microscopy. The whole volume of the derived data substantiates a prominent enhancement of the excess volume in the solidified ion tracks and the irradiation-induced modifications are discussed and analyzed in the framework of strong glass rejuvenation within the nanometric ion tracks.

1. Introduction

Metallic glass (MG) represents a class of materials that, owing to the disordered structure, exhibits unique physical and mechanical properties, such as high strength, toughness, and high (quasi-)elastic limit, thereby rendering it attractive for various applications. The effect of ion irradiation on MGs has been a subject of research in recent years, as these materials have potential applications as coatings in nuclear power plants, nuclear waste storage, aerospace, and other radiation-prone environments. The lack of a crystalline structure prevents conventional irradiation defects such as Frenkel pairs and dislocation loops, making MGs attractive candidates as structural materials under irradiation-prone conditions.

In addition to technological goals, previous studies have also investigated the fundamental interactions during the irradiation of metallic glasses. In this respect, the responses of MGs to different types of irradiation such as neutrons, electrons, or light ions in the kinetic energy regime of keV to tens of MeV have been studied. For example, nanopillar compression experiments explored the mechanical properties of ion-irradiated metallic glasses [1–4,5] and surface [6–8] and volume modifications [9,10] as well as irradiation-induced crystallization [5,11] were studied. In this energy regime, the electronic energy loss and the nuclear energy loss of incoming ions have comparable magnitudes, with the former being only a few times higher than the latter. Consequently, the dominant mechanism for radiation damage in this regime is primarily attributed to elastic collisions. The electronic loss component can have a competing defect annealing contribution, or a synergetic one and enhances the damage. So far, the range of irradiation with ions of higher masses and higher specific energies has not been explored for bulk metallic glasses and additional experiments focused on electronic-loss-driven damage mechanisms are required to complete the picture of ion-induced modification of metallic glasses. For this reason, swift heavy ion irradiation has been applied in this work. Swift heavy ion (SHI) is a special term applied for ions heavier than C, having a

---

specific energy above 1 MeV/u, corresponding to kinetic energies in the range of hundreds of MeV to GeV, which can be produced in large accelerator facilities [12]. For this regime, the predominant ion-stopping mechanism is the energy loss by excitation and ionization of the target atoms. It is important to note that the electronic energy loss greatly surpasses the nuclear energy loss by more than a factor of ten for the majority of the ion penetration depth (see Fig. 9 in the Supplementary section). Among several models suggested to describe the interaction of energetic ions with the matter, the thermal spike model described by Toulemonde [13] and Trinkaus and Ryazanov [14] provides the best explanation for the entire set of experimental observations including experiments on amorphous solids [15–17].

When a swift heavy ion penetrates a MG, a part of its kinetic energy is transferred to the electronic subsystem of the material on a femtosecond time scale. In the second step, this energy is thermalized and further transferred to the atoms via electron-phonon coupling. This process causes a local increase in temperature in a cylindrical volume around the ion trajectory that can exceed, for heavier ions with high stopping power, the melting point of the corresponding crystalline material of equal stoichiometry. This two-stage process is then followed by heat transfer to the surrounding cold matrix resulting in rapid quenching of the molten material. As a result, columnar structures which experienced a different thermal history as compared to the surrounding matrix are formed along the paths of the ions. Commonly these columnar regions are referred to as ion tracks. Based on their particular interaction mechanism with the target, leading to a very localized energy deposition, swift heavy ions can be used as a tool to modulate the properties of metallic glasses by generating high aspect ratio, nanometric trails consisting of a new disordered phase.

Previous research with SHI investigated the response of metallic glass ribbons and thin films, looking into aspects such as surface modifications and so-called "ion hammering" [18], free volume modifications and mechanical properties response [19], track etching and their morphology changes under stress [20] and also irradiation-induced crystallization [21,22]. The present study offers a comprehensive analysis of the effects of SHI irradiation on the thermodynamic, diffusional, mechanical, and microstructure properties of a model $Pd_{40}Ni_{40}P_{20}$ bulk metallic glass (BMG). SHI, or Swift Heavy Ion irradiation, serves as a valuable tool for investigating the energy landscape of this exceptional glass-forming system. It generates sufficient energy at the nanoscale to induce unique states and access various energy levels during the rapid quenching of the transient ion tracks.

2. Experimental

2.1. Sample fabrication and characterization

Bulk amorphous $Pd_{40}Ni_{40}P_{20}$ was produced using copper mold casting in a purified argon atmosphere with dimensions of $10 \times 30 \times 1$ mm^3 in cuboid form and also as cylindrical rods with a diameter of 5 mm. The alloy had been made using Pd plates and Ni_2P ingots, all with purities higher than 99.9%. The components were alloyed and premelted two times, once with B_2O_3 for further purification.

The amorphous state before and after irradiation has been verified by X-ray diffraction with a Bruker D-5000 X-ray diffraction (XRD) device applying Cu K_α radiation. The samples were cut into wafers and cuboids with a thickness of several hundred micrometers and were polished on two opposing sides to a mirror-like finish to provide a plane-parallel state. To eliminate the effect of quenching-related structural or compositional heterogeneities on the irradiation response, the samples have been annealed at 553 K for a duration of 60 min after polishing. The annealing time has been chosen according to a Kohlrausch-Williams-Watts (KWW) -type time dependence of structural relaxation of the as-quenched state and respective data values from the literature [23].

2.2. Ion irradiation

Samples were irradiated with 4.8 MeV/u ^{179}Au ions to total fluences in the range of 1×10^{11} to 5×10^{12} ions/cm^2 at the UNILAC accelerator, GSI Darmstadt. The effects of SHI irradiation on MGs also depend on the temperature and environment at which the irradiation takes place and also on the stopping power of the ion. At low temperatures, the irradiation-induced effects can be more easily preserved and accumulate over time, leading to a gradual modification of the structure and properties of the material. At high temperatures, on the other hand, the radiation-induced effects such as newly created excess volume can anneal out and the material can recover its original properties.

The temperature during the irradiation was monitored with a thermal camera, confirming that the temperature did not exceed 330 K. A low flux of 2×10^8 ions/cm^{2}s was used throughout the process. The calibrated ion beam was positioned normal to the surface of the samples and was homogenized to provide a consistent radiation condition.

For irradiation, cuboid-shaped samples were placed on an aluminum holder and were fixed by an aluminum bar, which also partially masked the sample. Additionally, a honeycomb mask was placed on the surface of the samples to partially mask the sample in a structured manner.

After irradiation, the wafers were thinned down from the backside to approximately 20 micrometers in thickness, which corresponds to the ion interaction range calculated by SRIM [24], see Fig. 9 in the Supplementary. Non-irradiated reference samples had been prepared by the same procedure. Samples that had been irradiated simultaneously, but without masking, were then used for calorimetric, low-temperature heat capacity, and diffusion measurements. Non-irradiated samples were analyzed as a reference if the respective reference state had not been analyzed earlier already. The cuboid samples were used for nano-indentation and surface analysis.

2.3. Analyses of structure and properties

Surface analysis has been performed by a Keyence VK-X3000 laser scanning microscope and a Bruker DektakXT profilometer. Differential scanning calorimetry (DSC) measurements were conducted with a Mettler Toledo DSC 3 device under a constant flow of 99.99% Ar gas with a flow rate of 20 ml/min. The disc-shaped samples had been thinned down to the penetration depth of the ions of 22 μm calculated by the SRIM MD simulation software. The approximate mass of the samples was 4 mg. To compensate for the small mass, 50 K/min was chosen as the heating rate. Low-temperature heat capacity measurements were performed in a physical property measurement system (PPMS, Quantum Design) under high vacuum conditions in the temperature range between 1.9 K to 100 K. The low-temperature heat capacity measurement is based on a $2 - \tau$ relaxation method which fits the temperature response to a defined heat pulse. Details of the method can be found elsewhere [25].

The diffusivity was determined by the radiotracer technique. The ^{110m}Ag radioisotope with a half-life of 249 days was purchased from Eckler & Ziegler. The radioactive solution was highly diluted in double-distilled water. The HNO$_3$-based acid solution has been directly deposited onto the surface of the specimen and was allowed to dry. The specimen was sealed in a silica tube under a purified Ar atmosphere and was annealed at 553 K for 17 days. An ion-beam sputtering technique has been applied for parallel sectioning, using a sputtering device developed by [26]. The total penetration depths were calculated by measuring the crater size and total weight loss of the sample with the known density under the assumption of a constant sputtering rate. The intensities of the γ-decays for individual sputtered sections were determined by a solid NaI γ-detector with a 16 K multi-channel energy discriminator which allows reliable measurement of the tracer penetration profiles without any effects of background radiation. Further details of the utilized radiotracer technique can be found e.g. in Ref. [27].

Nanoindentation has been performed using a FT-NMT04 IN-SITU SEM Nanoindenter. The indentation mapping employed a continuous stiffness measurement (CSM) in a displacement-controlled mode. All indentations have been done by a typical Berkovich diamond indenter and the maximum indentation depth was restricted to 200 nm. The area function of the tip and the device stiffness have been calibrated by indentation on a standard fused silica sample. The hardness and elastic modulus have been calculated using the Oliver and Pharr method [28–30]. Sample surfaces were polished using OPS prior to the irradiation.

The amorphous structure of the BMG was characterized after irradiation using fluctuation electron microscopy (FEM), since classical diffraction analyses such as X-ray diffraction or selected area electron diffraction (SAED) revealed no significant difference in the investigated samples that would explain the observations made by calorimetry or low-temperature heat capacity measurements [31–34].

Variable resolution fluctuation electron microscopy (VR-FEM) is a TEM-based method sensitive to the so-called medium range order (MRO) in disordered material due to its sensitivity to higher-order correlation functions. The measurements were conducted in a Thermo Fisher FEI Themis G3 60–300 transmission electron microscope operating at an acceleration voltage of 300 kV. Nano beam diffraction pattern (NBDP)s were acquired for different probe sizes in the range of 0.76 to 5.5 nm by adjusting the semi-convergence angle. To maintain consistent experimental parameters for the investigations, the following parameters were kept constant: thickness (45 nm), beam current (15 pA), and exposure time (4 s). The log-ratio method [35] was utilized using the low loss part of electron energy loss spectra (EELS) to determine the thickness of the analyzed regions. The FEM analyses were performed using the diffracted intensities $I(\rightarrow k, R, \rightarrow r)$ of sets of 100 individual NBDPs taken from a respective area.

In FEM, the statistical analysis of the variance $V(|\rightarrow k|, R)$ obtained from diffracted intensities of nanometer-sized volumes using STEM microdiffraction is quantitatively investigated [36–39]. FEM contains information on the pair-pair correlations and hence on the topological MRO [38,40–42].

The normalized variance $V(|\rightarrow k|, R)$ of the spatially resolved diffracted intensity I of a nanobeam diffraction pattern (NBDP) is described as a function of the scattering vector $\rightarrow k$ and the coherent spatial resolution R,

$$V(|\rightarrow k|, R) = \frac{\langle I^2(\rightarrow k, R, \rightarrow r) \rangle}{\langle I(\rightarrow k, R, \rightarrow r) \rangle^2} - 1 \tag{1}$$

where indicates the averaging over different sample positions $\rightarrow r$ or volumes, respectively, and R denotes the FWHM of the electron beam [43].

Sampling with different parallel coherent probe/beam sizes, R, is called VR-FEM [44,45]. It gives insight into the dominant structural correlation length scale(s) and provides a semi-quantitative measure for the MRO volume fraction (through the peak height and/or peak integral of the peak of the normalized variance as a function of the scattering vector). Thus, conclusions on the correlation length scale of the MRO can be drawn and can be correlated to macroscopically averaged properties of the amorphous material [38,41,45,46]. The MRO analysis performed here applies the Stratton-Voyles approach, assuming the dependence of the variance $V(\rightarrow k, R)$ on $1/R^2$. This analysis allows the separation of intercept- and slope-dominated parts of the correlation between normalized variance and probe size and allows analyzing the pair-pair correlation length of amorphous materials also for cases where different dominant MRO correlation lengths exist in one sample [46,47]. The uncertainty of the peak heights of the normalized variance signal was estimated from the absolute difference between the maximum measured peak height of the first peak of $V(\rightarrow k, R)$ and the amplitude of

a Gaussian function fitted to this first peak.

In this work, the MRO evolution upon SHI irradiation with up to 1×10^{12} ions/cm^2 in fluence was investigated. At such fluences, the probability of overlapping of the ion tracks is low, and the impact of track interactions is negligible. Transmission electron microscopy (TEM) samples have been prepared from the wafers by electropolishing, utilizing a TenuPol-5 electropolishing device with BK2 electrolyte [48] at 16.8 V and temperatures between $-20°$ to $-30°$C.

3. Results and discussion

3.1. Surface modifications

The first post-irradiation observation was focused on surface modifications. To partially mask the sample from irradiation, two kinds of masks have been used. A honeycomb mask of 100 μm thickness had been placed on the top of the samples and secured by copper tape before the irradiation. As shown in Fig. 1(a), a honeycomb pattern is observed after irradiation. All samples and masks were fixed on the sample holder by an aluminum bar that creates a solid, hard border between irradiated and non-irradiated regions across the sample.

The The Laser scanning microscopy (LSM) profile in Fig. 1(b) of the pattern indicated in Fig. 1(a) by the circular path indicates an out-of-plane and void-free (see Fig. 10 in the supplementary section)swelling step parallel to the incident beam. Fig. 1(c) shows a profilometry surface mapping of a sample irradiated by a fluence of 5×10^{11} ions/cm^2. The irradiated area at the border of the masks shows a large swelling step, as displayed in Fig. 1(d). Both LSM and profilometry have been utilized to cross-validate and establish the error bars in Fig. 1(d). This large swelling step increased by increasing the fluence and reached up to 100 nm. The deformation reaches a peak in the irradiated area towards the edge of the mask as a result of a plastic shear flow induced by large stresses at the interface between irradiated and non-irradiated material. This observation differs from the ion hammering effect previously observed for metallic glasses [49] where the sample dimension perpendicular to the ion beam grew, whereas the sample dimension parallel to the ion beam shrank while the mass density remained unchanged. The fact that ion hammering was not observed in our irradiation experiment conducted at approximately 300 K could be attributed to either the elevated temperature of our experimental setup or the achieved fluences being below the incubation fluence threshold for ion hammering. Higher shear viscosities of the bulk Pd$_{40}$Ni$_{40}$P$_{20}$ metallic glass in comparison with previously investigated amorphous alloys that had been vitrified at higher cooling rates would also hamper the ion hammering effect. The irradiated samples in this study are bulk samples, meaning that the ion beam does not penetrate the full thickness of the samples and the deformation of the irradiated areas is constrained by the un-irradiated part of the sample acting as substrate. Additionally the predominant deformation mechanism in the Pd$_{40}$Ni$_{40}$P$_{20}$ bulk amorphous alloy at temperatures well below the glass transition is shear banding, in contrast to Newtonian flow as assumed in the standard model of ion-hammering [49].

As mentioned before, a noteworthy effect visible in Fig. 1(a,b) is an overshoot (large swelling) in the vicinity of the mask, adding a 40 nm overshoot to the general swelling. This effect and a general smoothening of the surface hint towards a transient mobility at the surface of the irradiated sample, as a result of the electronic excitation near the surface by SHI irradiation during the ion track formation. The thermal expansion of the cylindrical region of the ion track creates a shear flow

$$\nu_x = 6R_p A_0 \Phi \sin\theta \cos\theta \tag{2}$$

where Φ is the ion flux, R_p is the penetration depth, A_0 is the deformation yield, and θ is the angle of the incident beam. After a time t this shear motion causes a net displacement of
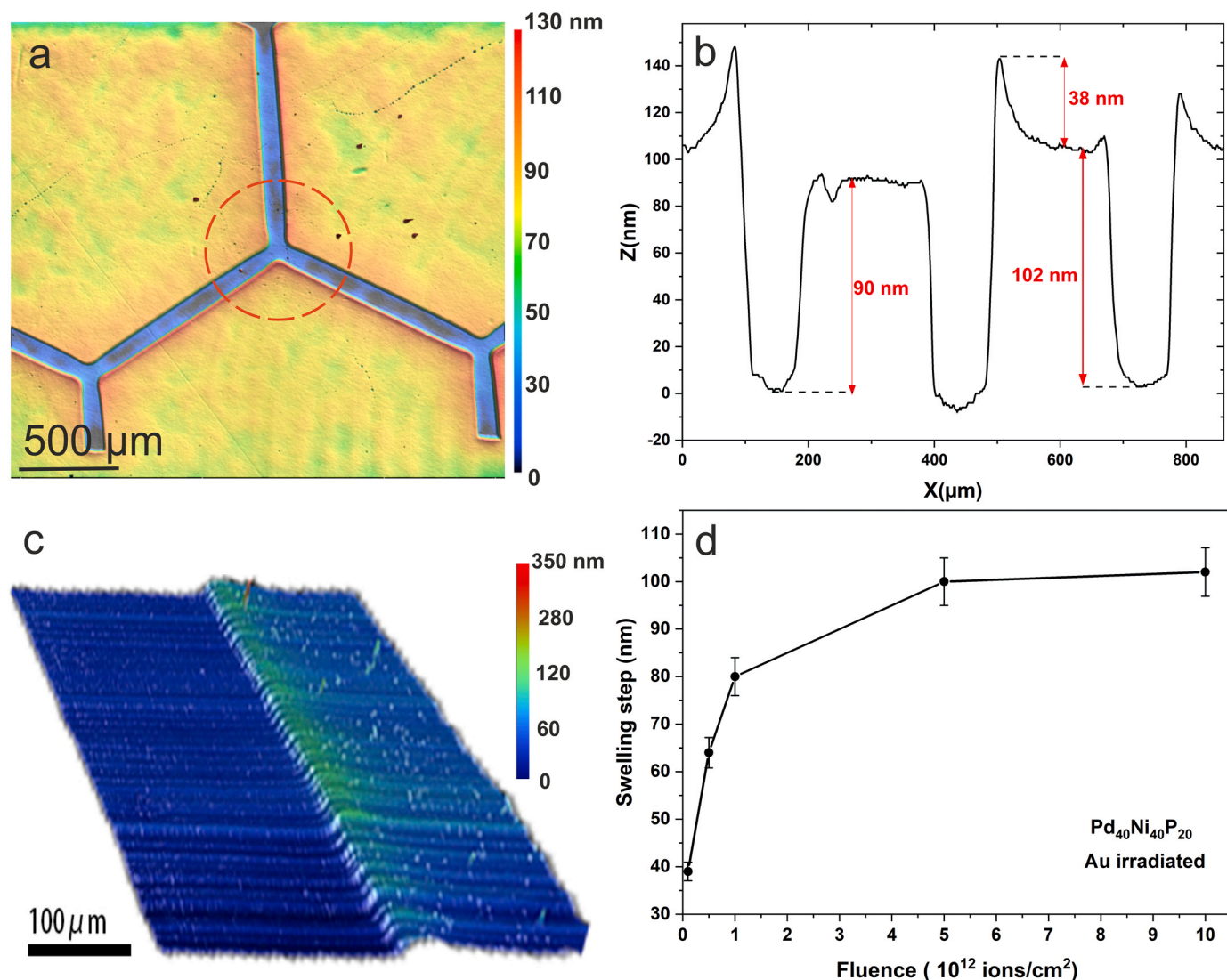
Fig. 1. Surface modification after irradiation, a) LSM image of the honeycomb pattern created by irradiation swelling on the surface at a fluence of 5×10^{12} ions/cm², b) surface profile of the circular pattern shown in a), c) profilometry surface mapping of a sample irradiated at 5×10^{11} ions/cm² and masked by the Al bar, d) evolution of the swelling step in dependence of the fluence.

$$\Delta x(z) = \nu_x t \qquad (3)$$

[14,50,51]. In this work the angle of the incident beam θ is nominally zero, however, any small variation and surface imperfection/roughness leads to the occurrence of this phenomenon.

3.2. Calorimetric analyses

DSC measurements and the subsequent enthalpy evaluation reveal that SHI irradiation effects are predominantly visible at temperatures below the glass transition. The corresponding changes of the enthalpy are referred to as "structural enthalpy", which is defined as the integrated DSC signal below the glass transition temperature (T_g). In this study, T_g was determined as 580 K and was unaffected by the irradiation.

Fig. 2(a) illustrates DSC heating scans of multiple samples heated up to 820 K at a fixed heating rate of 50 K/min. A systematic investigation of the pristine and irradiated states reveals that an increase in irradiation fluence consistently leads to a higher structural enthalpy. The sample with the highest irradiation fluence of 5×10^{12} ions/cm² exhibits the most significant structural relaxation signal (represented by the exothermic signals on the black curve in Fig. 2(a)) below T_g.

Furthermore, the endothermic overshoot at T_g, commonly known as enthalpy recovery [52,53] and commonly associated with a change in excess free volume, is also altered due to irradiation. At T_g, the endothermic overshoot decreases with increasing fluence, indicating a rejuvenating effect compared to the pristine glass. It is widely accepted that the enthalpy recovery is associated with α-relaxation processes. According to models describing metallic glasses MGs as a combination of soft and hard regions or regions with higher density, β-relaxation is related to atomic motion in the soft regions, while α-relaxation is connected to the hard or densely packed regions [54,55]. The reduction in enthalpy recovery indicates a softening of the hard or densely packed regions caused by irradiation. Fig. 2(b) provides an overview of the DSC scans, showing no modification of the crystallization peak after irradiation. The overall crystallization behavior remains largely unchanged, as evidenced by the unaffected crystallization enthalpy of (73 ± 3) J/g. No signs of partial (irradiation-induced) crystallization, which would manifest as a decrease in the crystallization enthalpy, are detected. The rejuvenation effect can be quantified by estimating the so-called fictive temperature as an indicator of the relaxation state in glassy materials and within the context of free-volume-based models [56], it serves as a measure for the relative amount of excess free volume stored in the material [57]. The changes in fictive temperature and structural
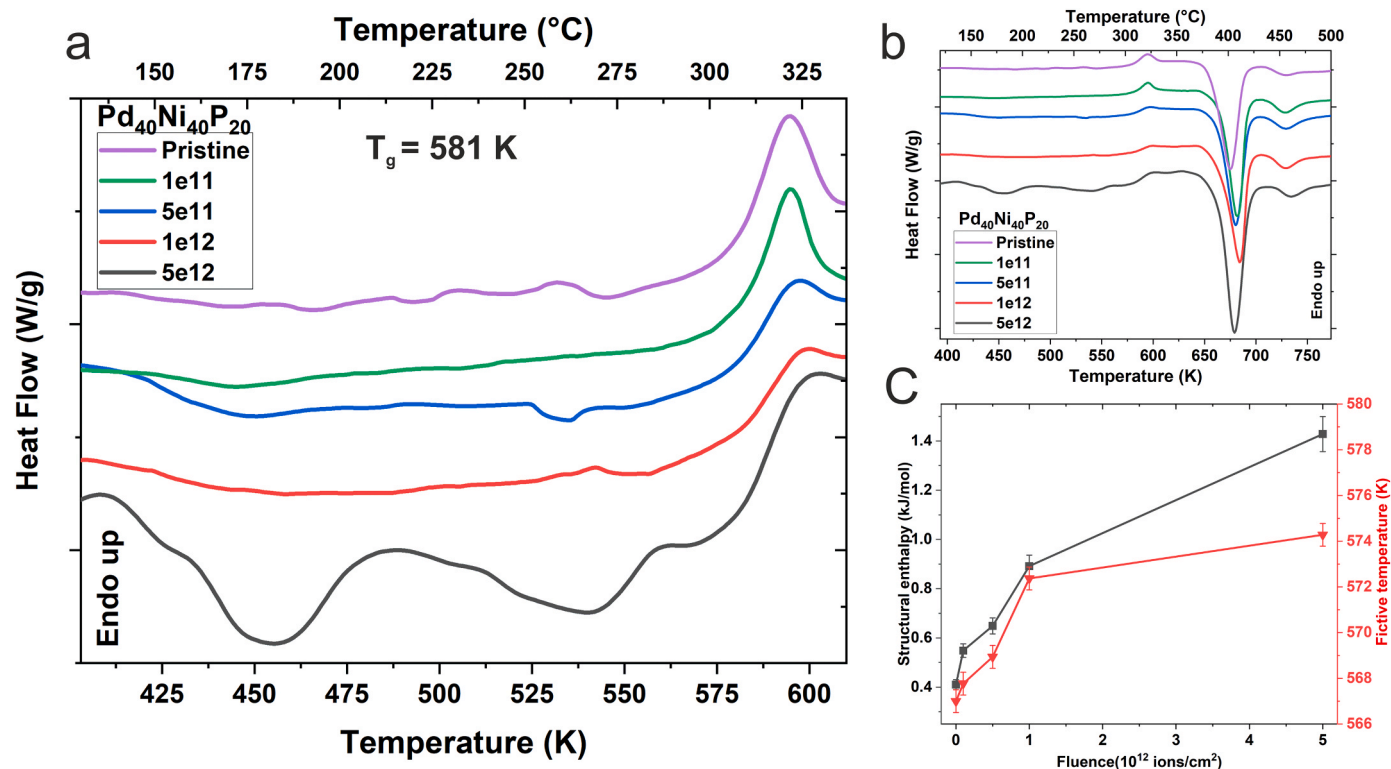
Fig. 2. DSC chart showing a series of DSC scans of the pristine (purple curve) and a series of irradiated materials. The heat flow is shifted by offset values for better visualization. a) DSC scans near the glass transition temperature, b) the full range of the DSC measurements including the crystallization transformation, c) changes of structural enthalpy and fictive temperature vs. irradiation fluence.

enthalpy are summarized in Fig. 2(c), where an increase in structural enthalpy corresponds to a shift towards higher values of the fictive temperature.

This behavior has been observed previously in mechanical deformation and thermal processing of metallic glasses [58,59] and is recognized as the so-called "rejuvenation" of the amorphous structure, which has been interpreted as introducing excess volume [60]. The macroscopic temperature of the specimens during irradiation was constant at around 330 K. The observed alterations in structural enthalpy and fictive temperature can thus be attributed to extensive structural rearrangements occurring as a result of the interaction with SHIs and involving initial track formation, resulting in a significant increase of the excess volume.

As previously discussed, according to the thermal spike model, the material inside/along the ion tracks is quenched at rates that are orders of magnitude faster than the cooling rate achieved during the synthesis of the pristine material. The extremely high quenching rate of the material within the ion tracks results in an amorphous structure with higher excess volume, which increases the structural enthalpy of the material.

Fig. 2(b) shows the crystallization peak of all states. The crystallization behavior does not show significant changes and the crystallization enthalpy remains unaffected at (73 ± 3) J/g. This is another indicator of the absence of crystalline volume fractions.

Glassy materials are known for exhibiting a characteristic low-frequency enhancement of the vibrational density of states causing deviations of the low-temperature heat capacity from the Debye law. This low-temperature excess heat capacity contribution is commonly referred to as the "boson peak". The boson peak is in the terahertz region of the vibrational spectrum and therefore influences the low-temperature heat capacity at temperatures of typically 5 to 50 K. According to the Debye law, the heat capacity for temperatures well below the Debye temperature consists basically of electronic and phononic contributions as:

$$C_p = C_p^{el} + C_p^{ph} = \gamma T + \beta T^3 \qquad (4)$$

The boson peak is analyzed by subtracting the electronic contribution from the total heat capacity and plotting C_p^{ph} vs. T^3 as shown in (Fig. 3).

The systematic study of the pristine state and different irradiated states shown in Fig. 3 (a), demonstrates a consistent increase of the boson peak as the irradiation fluence increased.

The changes in the boson peak upon rejuvenation and relaxation by mechanical deformation and annealing have been well demonstrated in previous studies [34,58,61,62]. It was shown that rejuvenation increases the boson peak amplitude, whereas relaxation or aging decreases it. It is accepted that the scattering of quasi-phonons at defective structures and structures with larger excess volume contribute to the boson peak [63].

Fig. 3(b) provides a summary of the boson peak changes including a gradual shift to lower temperatures by a maximum of $\Delta T = 2$ K. The uncertainties in determining the boson peak temperature have been assessed to be lower than ± 1 K. According to Shintani et al. [63] the boson peak temperature for less dense structures should increase since these structures have higher frequency components in their phonon spectrum. However, it has been shown in other studies that the boson peak temperature increases upon annealing and decreases upon plastic deformation [34,62]. The observed correlation of the boson peak height and temperature of the irradiated material aligns with the impacts of rejuvenation and enhancement of the excess volume reported previously [61]. In the current case, the most probable explanation for the enhancement of the boson peak strength and its observed correlation with the irradiation fluence would be the presence of the ion tracks which resemble hyperquenched regions exhibiting higher excess volume distributed in a heterogeneous manner throughout the bulk material.
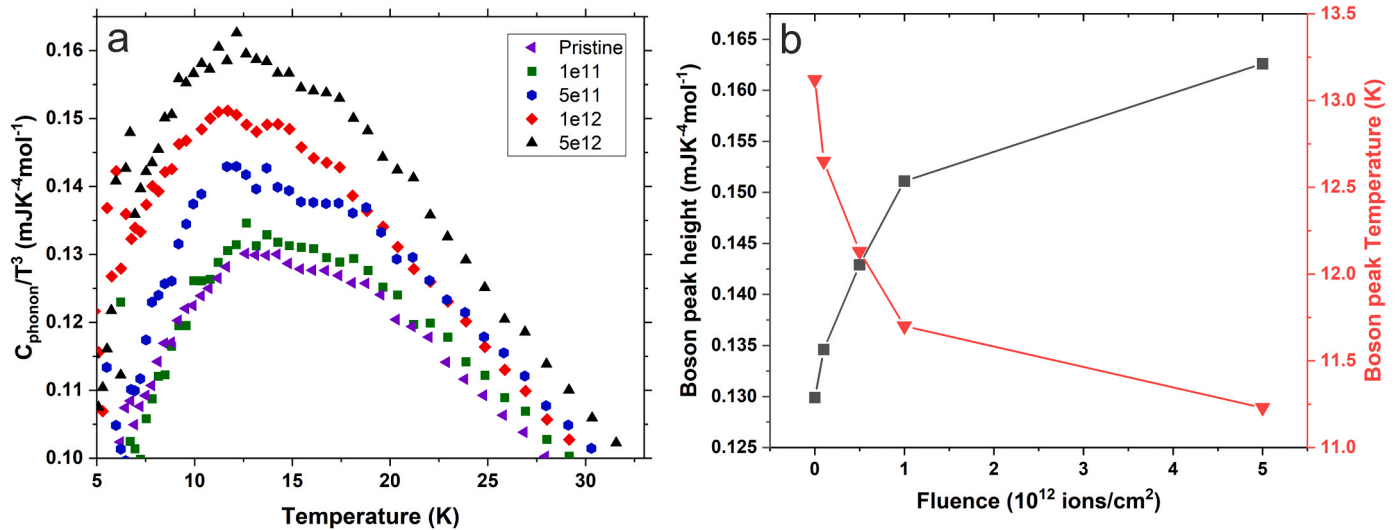
Fig. 3. a) Boson peak for the pristine and irradiated states, showing the increase of the boson peak height by the accumulation of fluence, b) changes of the boson peak height and temperature vs. fluence.

3.3. Radiotracer diffusion measurements

In the present work, tracer diffusion using the ^{110m}Ag radioisotope was measured in materials subjected to different ion fluences at a temperature of 553 K. The diffusion annealing time was chosen as 17 days. The annealing conditions (temperature/time) are selected to avoid any notable annealing-induced relaxation effects on the diffusion properties of the pristine material, as for instance observed by Duine et al [64] or Knorr et al. [65]. Thus, no prominent dependence (decrease) of the measured tracer diffusion coefficient, D^*, on the diffusion time t is expected for the selected conditions.

Fig. 4(a) shows the penetration profiles for the material irradiated by the four different fluences, including also a profile obtained on the pristine, non-irradiated material. Two effects are prominent: First, the penetration depths are drastically increasing from approximately 30 nm to more than 400 nm after irradiation. Given that the diffusion penetration depths are significantly smaller than the calculated ion

penetration depth of approximately 22 μm, it is reasonable to consider the energy loss as constant, resulting in uniform damage over the diffusion penetration depth. Second, the relative specific activity at the same penetration depth is higher in the material that had been irradiated with a higher fluence. Note that approximately the same total activity has been applied to the sample surfaces and allowed to diffuse.

The penetration profiles correspond to volume diffusion. However, two distinct branches are clearly distinguished in the profiles obtained on the irradiated states. Both branches follow a Gaussian-type behavior and the shallower (corresponding to larger depths) branch becomes more prominent with an increasing dose, Fig. 4(a). In the pristine, irradiation-free state, only one, steeper contribution is observed.

The profiles, $C(x)$, obtained on the irradiated material were fitted as a sum of two Gaussian-type contributions,

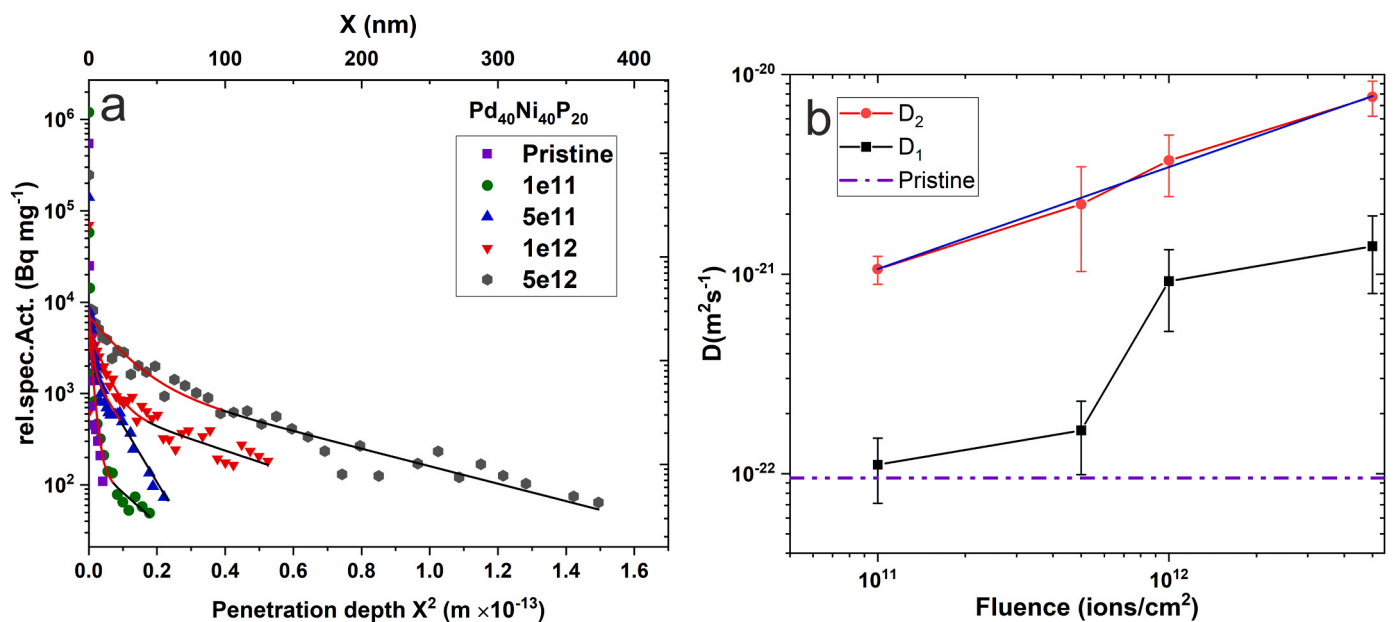$$C(x) = A_1\exp\left(-\frac{x^2}{4D_1 t}\right) + A_2\exp\left(-\frac{x^2}{4D_2 t}\right). \tag{5}$$

Fig. 4. (a) Penetration profiles of ^{110m}Ag in pristine and irradiated states, (b) Fluence dependence of the two diffusion coefficients. The purple line indicates the diffusivity of the pristine material.

Here C is the tracer concentration (which is proportional to the measured relative specific activity) at the depth x, D_1 and D_2 are the corresponding diffusion coefficients, A_1 and A_2 are the fit parameters, and t is the diffusion time. As it was mentioned, the penetration profile of the pristine sample was fitted by a single contribution, and solely D_1 was determined.

The determined tracer diffusion coefficients are presented in Fig. 4 (b) as a function of the total fluence. The diffusion coefficients corresponding to the faster (shallower) branch, D_2, which appears in irradiated samples, exceed the diffusion coefficients determined for the first branch, D_1, by at least an order of magnitude. The fluence dependence of the D_2 values is found to follow nearly a square-root dependence, $D_2 \sim \Phi^{0.51}$. On the other hand, the D_1 values are almost independent of the dose at lower fluences. The experimental data indicate a significant increase in the D_1 values between fluences of 5×10^{11} ions/cm² and 1×10^{12} ions/cm². This increase should not be perceived as a sudden change, nor should the fluence be regarded as a threshold. Instead, it is expected to occur gradually between the two mentioned fluences. Additional measurements at intermediate fluences could provide further clarity on the transition pattern.

As it was stated, a single volume diffusion branch – as it is expected – has been observed in the pristine state. The estimated D_1 value has a relatively large uncertainty in view of the extremely short penetration depth, below 30 nm, and due to the potential appearance of sputtering artifacts. However, in view of the systematical modifications of the penetration profiles with increasing fluence, we are considering the determined diffusion coefficients as reliable estimates. Moreover, as it has been shown by Duine et al. [64], the diffusivity of the as-quenched state decreases to an equilibrium value during the applied annealing treatment and longer annealing times increase the accuracy of the measurement.

The tracer diffusion coefficients, which are characteristic of the faster branch appearing in the irradiated samples, D_2, are likely to characterize the atomic transport within highly heterogeneous structures modified by the ion tracks. The diffusion enhancement is probably induced by an increased excess volume in the ion tracks. Moreover, the excess volume might be locally increased due to the overlapping of successive ion tracks resulting in enhanced diffusivities after irradiation at larger fluences. This hypothesis is also in line with a systematically higher activity measured at the same penetration depths for the samples irradiated at higher fluences, which could be related to the increased number density of the ion tracks in the material.

The atom diffusion rates in MGs were suggested to be explained in terms of the free volume model [56,66–68]. In this approach, the tracer diffusion coefficient, D, is written as [69],

$$D = \gamma a^2 f \nu c_d \exp(S/k_B)\exp(-Q/k_B T) \tag{6}$$

where c_d is the "free-volume-type defect" concentration, in fact, the central parameter of the model. γ is a geometric factor, f is a correlation factor, ν is the jump attempt frequency, S is the diffusion entropy, Q is the diffusion activation energy, and k_B is the Boltzmann constant and T the temperature [70]. The diffusion defect concentration, c_d, is approximated as $\exp(-\alpha\Omega*/\Omega_f)$ from the free volume theory, here Ω_f is the average amount of excess volume, $\Omega*$ is the critical volume to create a diffusion defect, and α is an overlap factor. The equilibrium defect concentration for $Pd_{40}Ni_{40}P_{20}$ glass, c_d^0 was estimated to be of the order of 10^{-6} applying the flow defect model [67,69].

SHI irradiation increases the excess volume, Ω_f, and we may write $\Omega_f = \Omega_f^0(1 + \Delta)$, where Ω_f^0 is the excess volume in quenched and equilibrated glass (considered as a reference) and Δ is the relative change (an increase is expected) of the excess volume induced by irradiation. Assuming that the irradiation enhances the excess volume in the glass while other parameters remain approximately not affected, the ratio of the measured diffusion coefficients, $D_{1,2}$ to that in pristine (equilibrated,

not-irradiated) glass, D_p is

$$\frac{D_{1,2}}{D_p} = \exp\left(-\frac{\alpha\Omega*}{\Omega_f^0}\left(\frac{1}{1+\Delta} - 1\right)\right) \tag{7}$$

where $D_{1,2}$ is the diffusivity corresponding to either first, D_1, or second, D_2, branch in the profile measured on irradiated samples. Equation (7) can be re-written as,

$$\frac{\Delta}{\Delta + 1} = \frac{-1}{\ln(c_d^0)}\left(\ln\left(\frac{D_{1,2}}{D_p}\right)\right) \tag{8}$$

Using Eq. (8), the values of Δ_1 and Δ_2 are estimated from the measured values of D_1 and D_2 shown in Fig. 4(b). Fig. 5 represents the estimated values of the relative excess volume, Δ, as a function of fluence.

The excess free volume Δ_2, which is considered to be characteristic for the glassy material directly affected by ion tracks, is seen to increase with increasing fluence according to $\Delta_2 = 0.171 + 0.0368\ln(\Phi/\Phi_0)$, where $\Phi_0 = 10^{12}$ ions/cm² and reaches the value of about 30% for the fluence of 5×10^{12} ions/cm². Almost no changes of the excess volume are seen in the areas between track centers at low fluences, below 10^{12} ions/cm², as suggested by the D_1 values, and it starts to increase at high fluences. One can directly show that this logarithmic dependence is translated to almost a square-root dependence of the tracer diffusion coefficient D_2 on the fluence derived previously, i.e. $D_2 = 2.36D_p\cdot\left(\frac{\Phi}{\Phi_0}\right)^{0.0368\alpha\Omega*/\Omega_0} \approx 2.36D_p\cdot\left(\frac{\Phi}{\Phi_0}\right)^{0.51}$.

The estimated values of the excess volume are very reasonable; however, the absolute values have to be considered carefully as they rely on the approximations used. Thus, in Fig. 5 the trends are discussed which can be used as an upper limit for the excess volume changes corresponding to Eq. (6).

Since one may expect a certain evolution of the excess free volume during the diffusion annealing (that corresponds to a time-dependent diffusion coefficient), the D_2 values represent in this respect *effective* diffusion coefficients.

An increase of the D_1 values at high fluences, Fig. 4(b), or accordingly an increase of the relative excess volume Δ_1, Fig. 5, correspond probably to a threshold value when different ion tracks begin to overlap. As a result, the irradiated glassy material remains heterogeneous, with heavily distorted (multiple track cores overlapping) and relatively less
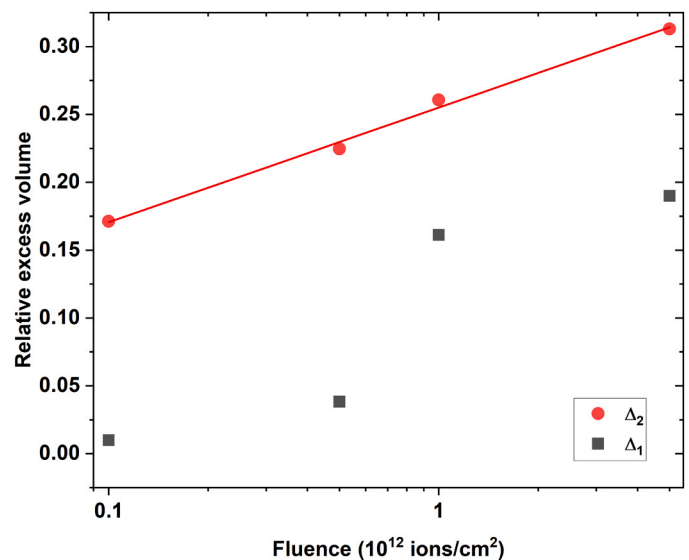

Fig. 5. Excess volume in irradiated samples with respect to that in the pristine, irradiation-free sample as a function of fluence. The two values, Δ_1 and Δ_2 were estimated by applying the concept of free volume-based defect concept to the measured diffusion rates D_1 and D_2, respectively.

distorted (probably single ion tracks) regions. Note that at highest fluences, the D_1 values correspond to those which are characteristic for the fast branches at a lower fluence of 10^{11} ions/cm^2, Fig. 4(b). The diffusion data indicate that the overlapping of the ion tracks begins at a threshold fluence, Φ_{th}, of about 3×10^{11} ions/cm^2. This value corresponds to an average diameter of the tracks of about $1/\sqrt{\Phi_{th}} \sim 20$ nm.

It is important to acknowledge that the influence of relaxation on diffusion rates occurs primarily in the irradiated part of the material. Previous research has demonstrated that ion tracks in metallic glasses can fully recover when heated to the supercooled liquid region [71], indicating that a partial relaxation at lower temperatures is also plausible. However, the diffusion coefficients reported in the present work are effective values, estimated as $\overline{D} = \frac{1}{\tau} \int_0^\tau D(t)dt$, where τ is the total annealing time. Consequently, the primary objective of this study is not to provide solely the absolute values for the diffusion coefficients, but rather to compare the measured data with those of the well-defined relaxed pristine state. A study of the relaxation behavior of the irradiation-modified dynamics in a glass might be a goal of a separate study.

3.4. Mechanical properties

The effects of structural rejuvenation induced by SHI irradiation on the micromechanical behavior have been investigated by nano-indentation. Fig. 6(a,b) shows a high-resolution nanoindentation map of hardness and Young's modulus after irradiation at the highest fluence of 5×10^{12} ions/cm^2. The area in the middle is an area shielded from irradiation by the honeycomb-shaped mask. It is clearly visible that the irradiation has caused a significant decrease in hardness and elastic modulus. Fig. 6(c) shows the hardness and elastic modulus after irradiation with four different fluences. It is evident that the accumulation of fluence affects mechanical properties. With increasing fluence the hardness as well as the Young's modulus decreases.

The hardness of MGs is directly related to their flow stress [72]. The plastic deformation in MGs occurs through the activation of shear transformation zones (STZs) [73,74], and the behavior of these STZs is greatly influenced by the presence of excess free volume within the material. Previous research has shown that relaxation processes and the reduction of excess volume contribute to an increase in hardness in MGs [75,76]. Consequently, the observed decrease in hardness can be attributed to the generation of excess volume, which is likely a result of track formation in the material.

Other important information that can be gained from the nano-indentation are the ratios H/E_r and H^3/E_r^2 known as wear resistance and yield pressure, respectively. Here H is the hardness and E_r is the reduced Young's modulus. The wear resistance that is also referred to as the "plasticity index" is a measure to determine the limit of the elastic behavior on a contact surface. The yield pressure is representative of the material's resistance to plastic deformation under loaded contact [77, 78].

A summary of the values for all conditions is provided in Table 1. The values of wear resistance do not change significantly after irradiation but show a slight decrease when comparing lower (1×10^{12} ions/cm^2) to higher 5×10^{12} ions/cm^2 fluences. The yield pressure also shows the same trend, as it decreases with increasing fluence.

Fig. 6(e) shows individual indentation imprints from the masked and irradiated area, indicated in Fig. 6(c). The masked area shows numerous shear bands in the form of pile-ups around the indentation imprint. Interestingly, discrete pile-up and shear bands are barely visible on the
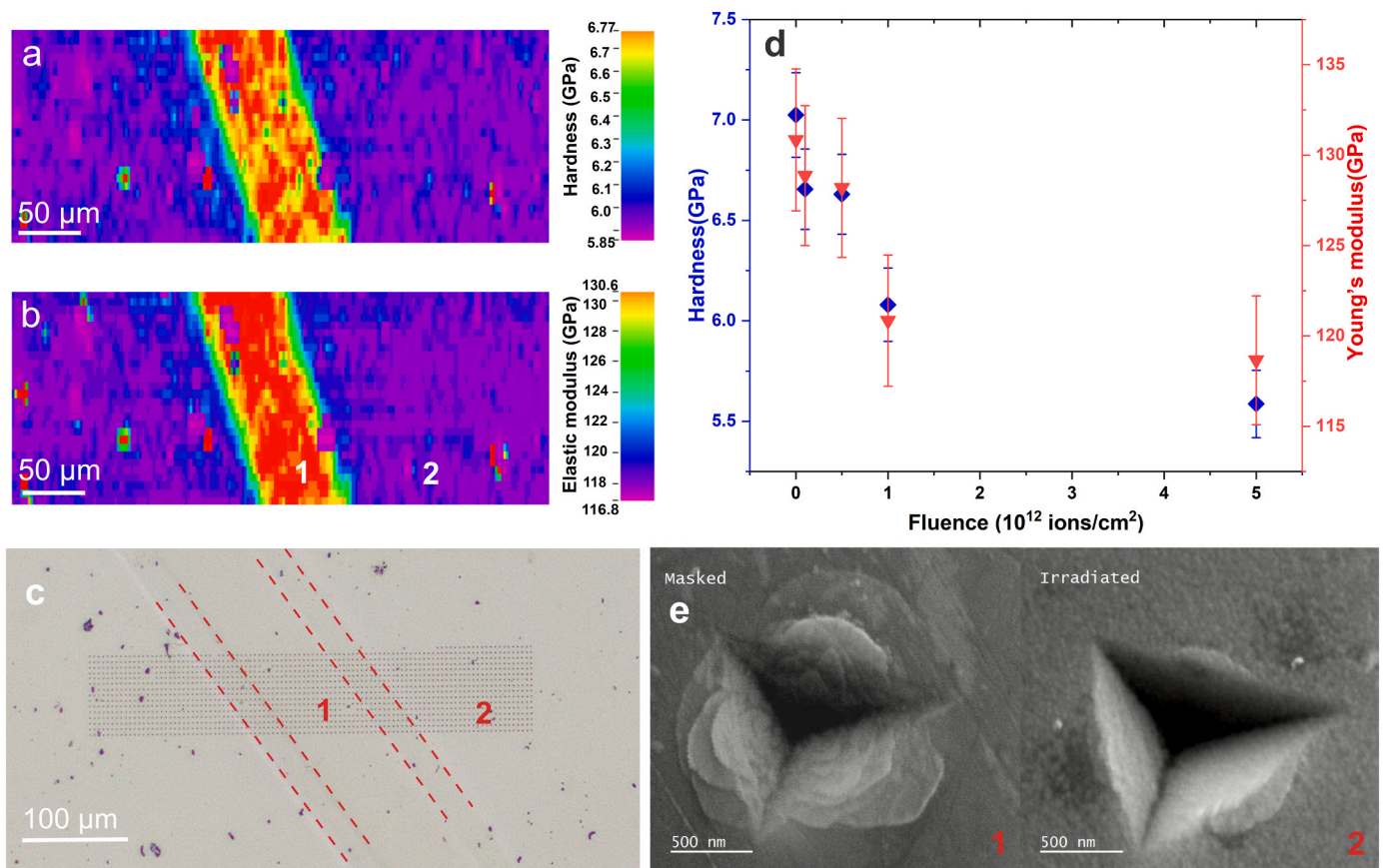

Fig. 6. a) and b) high-resolution hardness and elastic modulus indentation maps for an irradiation fluence of 5×10^{12} ions/cm^2, c) optical image of the indentation array the lines show the border of the mask and the region of swelling overshoot, d) the evolution of hardness and elastic modulus with irradiation fluence, e) SEM image of the indents from the masked and irradiated region of the array shown in c).

Table 1
Summary of values of H/E_r and H^3/E_r^2.

Sample		H/E_r	H^3/E_r^2 (GPa)
Pristine		0.053 ± 0.001	0.020 ± 0.001
1×10^{11}	ions/cm^2	0.051 ± 0.001	0.017 ± 0.001
5×10^{11}	ions/cm^2	0.051 ± 0.001	0.017 ± 0.001
1×10^{12}	ions/cm^2	0.050 ± 0.001	0.015 ± 0.001
5×10^{12}	ions/cm^2	0.047 ± 0.001	0.012 ± 0.001

irradiated side. The absence of shear bands can be correlated to the structural changes, i.e. to the increase of the excess volume which favors viscous plastic flow (homogeneous deformation) without distinct shear localization [79].

The observed elastic modulus changes by SHI irradiation can be interpreted as being due to irradiation-induced defects with high excess volume in the ion tracks, which eventually increase the overall excess volume in the material. Since the elastic modulus is determined by the interatomic interaction potential, an increase of the number density of irradiation-induced defects induces a reduction of its value. Concomitantly, the observed hardness reduction by nearly 18% is also a consequence of the same phenomenon, which is more pronounced than the reported mechanical softening caused by profuse shear banding [80] and residual stresses [81]. The observed elastic modulus changes by SHI irradiation can be interpreted as being due to irradiation-induced defects with high excess volume in the ion tracks, which eventually increase the overall excess volume in the material. Since the elastic modulus is determined by the interatomic interaction potential, an increase in the density of irradiation-induced defects induces a reduction of its value. Concomitantly, the observed hardness reduction by nearly 18% is also a consequence of the same phenomenon, which is more pronounced than the reported mechanical softening caused by profuse shear banding [80] and residual stresses [81]. Additionally, the quenched-in ion tracks may act as soft nanometric heterogeneities that tend to yield earlier and could act as nucleation sites for a larger number of shear bands [82], which can accommodate the applied strain more effectively. Similar behavior has been found in molecular dynamics simulations on shear band multiplication mechanisms in a heterogeneous metallic glass consisting of two distinct amorphous regions with different amounts of free volume and degrees of short-range order. [83]. The generation of a high density of shear bands with a regular pattern, which interacts with each other and with the ion tracks, would enhance the plasticity and hinder an early failure of the SHI-irradiated BMG [84]. It is important to note that this mechanism is different from the pinning of dislocation motion by defect aggregates formed within the ion tracks, leading to the hardening of SHI-irradiated crystalline materials [85–87].

3.5. Structure response of metallic glass to irradiation

FEM measurements have been conducted to obtain metrics on the local atomic correlations in the glass [45]. The FEM signal height contains information about the MRO volume fraction. Various studies on Pd- and Zr-based glasses have demonstrated that treatments and processings such as thermal treatments, severe plastic deformation, and minor alloying have a notable effect on the MRO and thus on the materials' properties [61,88–90].

The relationship between MRO and the second nearest-neighbor atomic structure is crucial for understanding the structural correlations in the amorphous state. The term medium-range order (MRO) is commonly used by theoreticians to refer to the atomic structure that extends just beyond the nearest neighbor atom shell, which is formed by density fluctuations. Here, the term is used as topological MRO, which describes atom-atom correlations beyond the nearest neighbors. In this context, MRO correlation lengths are typically proposed to be within the range of approximately 1 to 4 nm [32,37,91,92] or generally larger than 0.5 nm [93], which is the length scale used to describe short-range order.

In this work, the MRO evolution upon SHI irradiation up to 1×10^{11} ions/cm^2 fluence was investigated. At such fluence, the probability of overlapping of the ion tracks is low and thus, the impact of track interactions is negligible.

To reach a deeper understanding of the influence of SHI irradiation on the MRO, the VR-FEM results of different treatments are compared in Fig. 7, namely as-cast, annealed at 561 K, and severely deformed after annealing at 553 K, taken from Ref. [23,61,90] respectively. The as-cast and annealed (561 K) state represent a well-defined pristine reference state. The deformed state serves to provide a comparison to a rejuvenated glass obtained by confined deformation.

The FEM results for all investigated states shown in Fig. 7 are displayed in the form of Stratton-Voyles plots [47]; that is, V_{first} at $k = 4.8$ nm^{-1} plotted against $1/R^2$. The corresponding R values are displayed on the upper scale of the x-axis. The MRO volume fraction, as obtained from the height of the normalized variance peak, describes the amount of matter that contributes to structures characterized by a given correlation length as obtained from VR-FEM. Changes of the excess (free) volume are changing the entire volume of the material. Thus, a glassy material can have a larger fraction of the particles (i.e. the atoms in this case) being situated in space in such a way that they contribute to a certain correlation length(i.e. *a* certain MRO) but still, the average distance between the particles might be enlarged (signifying enhanced excess volume). In this sense, changes of the excess free volume are reflected in the k-values of the maxima of the normalized variance peaks while the MRO fraction affects the amplitude of these maxima. Although there may be correlations between the two, they are not causally linked. In view of structural models of (metallic) glasses, e.g. involving a "rigid backbone" and "energetically unfavorable motifs", the correlation between total volume, total excess volume, and MRO becomes even less obvious, as different partial systems of the entire structure might contribute differently to the different properties.

Within the error bars, all curves show a similar trend. There is a monotonously increasing FEM signal with decreasing probe size. Thus it can be concluded that the correlation length is not significantly different in all four states. There is an indication for a plateau at about (2.8 ± 0.5) nm similar to the one at (3.1 ± 0.6)nm for the as-cast sample (Fig. 7(a)) but not for the pristine or annealed and deformed sample (Fig. 7(b)). This observation (plateaus) has been interpreted as the presence of two MRO different correlation lengths or two different MRO networks [46, 89]. Moreover, the degeneration of the plateau at larger probe sizes in the pristine sample (Fig. 7(b) seems to be a result of the annealing treatment and also correlates with the reduction of excess volume [94]. However, this plateau reappears after irradiation and is even more extended in width, indicating an increased heterogeneity of the MRO. Moreover, it is noticed that the normalized variance of the irradiated sample (1×10^{11} ions/cm^2) is generally higher than in the other curves indicating a higher MRO volume fraction.

Notably, both severe radiation and severe deformation did not significantly change the position of the first plateau at about (1.2 ± 0.3) nm and thus the correlation length of the MRO. However, there seems to be a general trend that irradiation increases the MRO volume fraction slightly.

Finally, it is important to mention that high-resolution transmission electron microscopy (HR-TEM) did not definitively detect contrast variations caused by ion tracks (see Fig. 10 in the supplementary section). While direct observation of the ion track has not been accomplished, alternative methods such as Small-Angle X-ray Scattering (SAXS) hold potential in offering substantial evidence in this issue [20,21].

In crystalline materials, irradiation induces Frenkel- or interstitial vacancy pairs when atoms are displaced from their lattice sites. Meanwhile, in MGs the defects are in the form of a pair of excess volume defects and its counterpart, an interstitial-type or "anti-excess volume" defect [95]. It should be noted that in the original work, the term "free" volume instead of "excess" volume has been used. As the term "free"
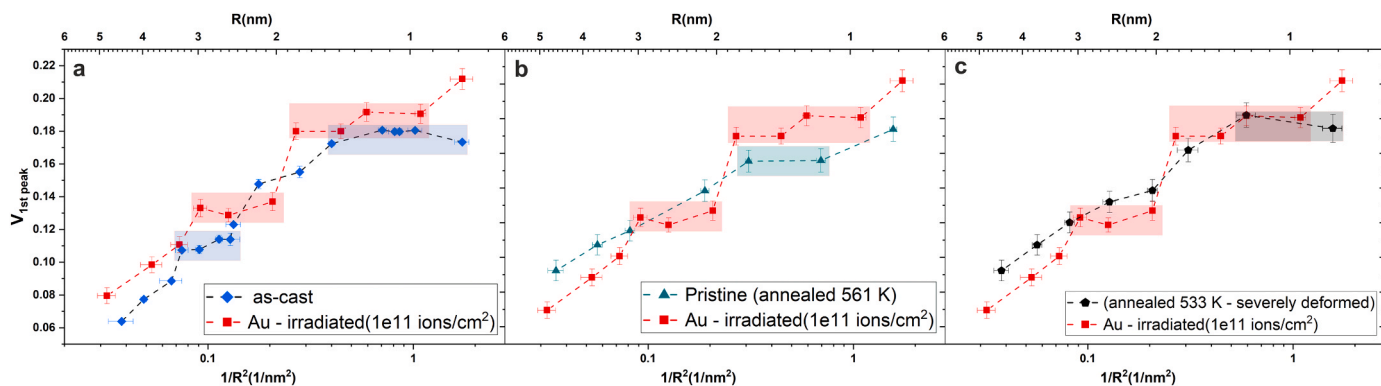
Fig. 7. FEM analyses of differently treated $Pd_{40}Ni_{40}P_{20}$ BMG displaying V_{first} at $k = 4.8$ nm^{-1} plotted against $1/R^2$. The corresponding R values are displayed on the upper scale of the x-axis. a) Comparison of the as-cast and irradiated state, b) Comparison of the state after annealing at 561 K with the irradiated state, c) Comparison of the irradiated state with a state experiencing pre-annealing at 553 K and high-pressure torsion deformation (10 rotations, $\epsilon_{eq} = 90\%$). The data for non-irradiated states are taken from Ref. [23,61,90]. Plateaus are indicated by the colored boxes.

volume implies specific conditions that hold only for a fraction of the excess volume, according to the free-volume models [56,96,97], we refer here to the additional volume as "excess" volume. In the case of

SHI, these defects and the resulting density fluctuations are assumed to be concentrated in the ion tracks.

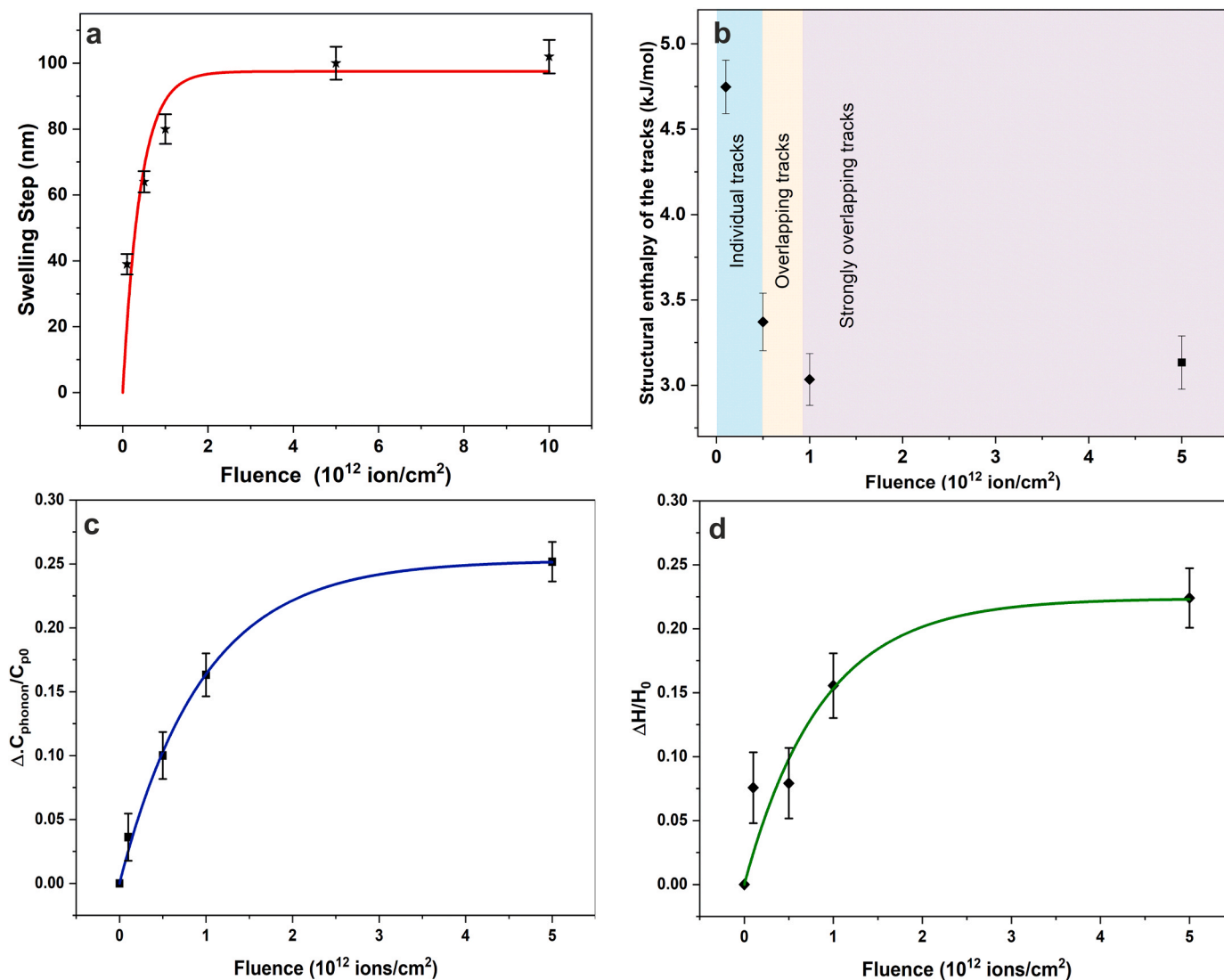The damage under SHI irradiation in many materials, including

Fig. 8. a) Fit of the direct-impact model to the experimental data of the swelling step, b) structural enthalpy of the ion tracks, c, d) The fit of the direct-impact model to the experimental data of the relative change of hardness and the relative change of the boson peak strength, respectively.

metallic systems can be described by a direct-impact mechanism [98,99] where the overall damage results from the accumulation and over-lapping of the individual tracks. In this framework, the damage fraction f is given as:

$$f = f^{sat}[1 - \exp(-\sigma\Phi)] \qquad (9)$$

where f^{sat} is the damage fraction at saturation, σ is the damage cross section, and Φ is the irradiation fluence. The fit of the damage fraction to the experimental data can be used to calculate the damage cross-section. Fig. 8 shows the fitting of the experimental data of the swelling step. The damage cross section determined from the model fit of swelling is $\sigma = (241 \pm 40)$ nm^2, with a track radius of $r = 8.75 \pm 3$ nm. This evaluation is in agreement with the track radius determined from the diffusion measurements of ~ 10 nm. The model can also be applied to changes in hardness and the boson peak using the relative changes in these two quantities, as depicted in Fig. 8(c,d). Through the fitting process, the values of the damage cross section are determined as $\sigma = (115 \pm 40)$ nm^2 and $\sigma = (107 \pm 10)$ nm^2 respectively. These values subsequently yield track radius values of $r = 6.01 \pm 3$ nm and $r = 5.75 \pm 2$ nm. Although these values are smaller than those obtained from swelling data and diffusion, they are still in good agreement with the previous estimations, taking the error bars into account. It is important to note that observing the morphology of ion tracks in MGs can be challenging, especially in cases where crystallization or phase separation is not present. This difficulty stems from the lack of a crystalline structure and the unique characteristics of ion tracks in these systems. The ion tracks represent a modified amorphous state within another amorphous matrix, making it unlikely to observe a track solely due to elemental or density fluctuations. Despite the absence of direct observational evidence, the consistent estimation of damage cross-section values across several experimental data and the application of two distinct models provide greater confidence in the reliability of of the evaluation the irradiation effect and its underlying mechanism.

The damage cross-section and track radius, determined in the current analysis using the direct impact model and diffusion data, surpass some values previously reported for crystalline materials [20,100,101]. Nevertheless, they align with values achieved for ion tracks in metallic glasses, such as FeB, FeBSiC, and FeNiB, at comparable ion energy-loss values (60 keV/nm), as evidenced by SAXS and resistivity data [102, 103]. This observation can be discussed within the framework of electron-phonon coupling. Metallic glasses generally exhibit significantly larger electron-phonon coupling [104–106]. Additionally, metallic glasses have lower melting temperatures compared to their pure constituents and most crystalline alloys. These factors collectively contribute to reaching the melt phase and forming larger ion tracks when the energy threshold is reached. Formation of the track requires a certain electronic energy loss threshold which strongly depends on the material under irradiation. MGs are among materials that are less sensitive to radiation and require a higher threshold for track formation. To estimate the threshold in this study, we referred to the observation of material response to lighter ions of Ca and Xe (not presented here). Irradiation with Ca did not cause swelling but irradiation with Xe-ions caused noticeable swelling. Therefore the threshold should lie between the energy losses of these two ions and was conservatively chosen to be 25 keV/nm. Based on this threshold, the effective depth of the material modified by the Au ions was calculated as 15 nm. Assuming that the density changes are negligible, the effective irradiated mass portion of the sample has been calculated. It is important to mention that the values of the structural enthalpy in Fig. 2(c) represent signals from the relaxation of the rejuvenated structure of the ion track as well as their surrounding matrix. By calculating the total irradiated surface according to the values of the damage cross-section and using Eq. (9) and under the assumption that the density changes are negligible, the effective irradiated mass portion of the sample can be calculated. Fig. 8 (b) shows the normalized enthalpy of the tracks. For primary tracks at low fluences, the chance of overlapping of the tracks is lower. At higher fluences the effect of overlapping starts and finally reaches saturation values at around 10^{12} ions/cm^2. Here, a comparison can be made between the rejuvenation by SHI and cryogenic cycling. Cryogenic cycling has been observed to induce rejuvenation and structural enthalpies in Zr-,La-,and Pd-based glasses [107,108]. The structural enthalpies reported by this method are between 0.6 and 1.1 kJ/mol. In comparison to the values presented in Fig. 8(b), SHI irradiation seems to produce a stronger effect which is an indication of the strong heterogeneity produced in the ion tracks.

These results signify the strong rejuvenation potential offered by irradiation with swift heavy ions, rendering this method a candidate approach for the structural engineering of metallic glasses at the nanoscale. It is crucial to highlight that when an ion collides with a target, its primary effect is a thermal spike, which primarily manifests as a thermal effect. This thermal spike leads to a rapid quenching of the affected trajectory within picoseconds, resulting in an increased excess free volume content within the system. While the term "rejuvenation" is used, it is important to acknowledge that the irradiation from SHI leads to the formation of a new nanoscale glass with a higher excess volume content.

4. Conclusions

Structural rejuvenation of a BMG has been achieved by SHI irradiation. It was shown that the diffusivity in the irradiated material was enhanced by 1 – 2 orders of magnitude with respect to the pristine material. The damage cross-section has been estimated by quantitative analysis of the swelling, allowing the evaluation of the structural enthalpy of the ion tracks.

The observed mechanical softening after irradiation can be explained by irradiation-induced structural rejuvenation, which is matched by the increasing structural enthalpy and fictive temperature. Both are in line with an increase in excess volume also elaborated from the results of tracer diffusion measurements.

Changes in the MRO correlation length are also noticeable. There is an indication for a structural re-occurrence of states induced by ion irradiation. Irradiation and deformation show similar trends for structural developments. Moreover, there is a slight but noticeable increase in MRO volume fraction after irradiation.

The tracer diffusion measurements revealed a distinct contribution of the ion tracks, allowing an estimation of the increase of the excess volume fraction by an upper limit of about 30% for an irradiation fluence of 5×10^{12} ions/cm^2.

SHI irradiation thus has been shown as a promising method to tailor the amorphous structure of MGs, as it allows for controlled and precise modification of the structural and relaxational properties of amorphous materials on the nanoscale. Moreover, the comparison with severely deformed states of the identical glassy material indicates that irradiation with swift heavy ions creates more "extremely" rejuvenated states enabling exploration of so far uncharted regions of glassy structures and glassy dynamics.

CRediT authorship contribution statement

S. Khademorezaian: Writing – review & editing, Writing – original draft, Visualization, Validation, Methodology, Investigation, Formal analysis, Data curation, Conceptualization. **M. Tomut**: Writing – review & editing, Writing – original draft, Validation, Supervision, Resources, Project administration, Conceptualization. **M. Peterlechner**: Writing – original draft, Validation, Supervision. **M. W. da Silva Pinto**: Writing – review & editing, Investigation, Data curation. **H. Rösner**: Writing – review & editing, Writing – original draft, Validation, Supervision, Methodology, Investigation. **S. Divinski:** Writing – review & editing, Writing – original draft, Validation, Supervision, Data curation, Conceptualization. **G. Wilde**: Writing – review & editing, Writing –

original draft, Validation, Supervision, Resources, Project administration, Funding acquisition, Data curation, Conceptualization.

Declaration of Competing Interest

The authors declare the following financial interests/personal relationships which may be considered as potential competing interests: Saba Khademorezaian reports financial support was provided by German Research Foundation.

Data availability

Data will be made available on request.

Acknowledgements

Appendix A. supporting information

Supplementary data associated with this article can be found in the online version at doi:10.1016/j.jallcom.2024.173571.

References

[1] R. Raghavan, et al., Ion irradiation enhances the mechanical performance of metallic glasses, Scr. Mater. 62 (7) (2010) 462–465, https://doi.org/10.1016/j.scriptamat.2009.12.013.

[2] R. Raghavan, et al., Nanoindentation response of an ion irradiated Zr-based bulk metallic glass, Mater. Sci. Eng. A 532 (2012) 407–413, https://doi.org/10.1016/j.msea.2011.11.004.

[3] D.J. Magagnosc, et al., Effect of ion irradiation on tensile ductility, strength and fictive temperature in metallic glass nanowires, Acta Mater. 74 (2014) 165–182, https://doi.org/10.1016/j.actamat.2014.04.002.

[4] B. Zhu, et al., Enhanced ductility in Cu64Zr36 metallic glasses induced by prolonged low-energy ion irradiation: a molecular dynamics study, J. Alloy. Compd. 873 (2021) 159785, https://doi.org/10.1016/j.jallcom.2021.159785.

[5] T. Liu, et al., Indirectly probing the structural change in ion-irradiated Zr-based metallic glasses from small scale mechanical tests, Intermetallics 121 (2020) 106794, https://doi.org/10.1016/j.intermet.2020.106794.

[6] H. Narayan, et al., An SEM and STM investigation of surface smoothing in 130 MeV Si-irradiated metglass MG2705M, J. Phys. Condens. Matter 11 (13) (1999) 2679–2688, https://doi.org/10.1088/0953-8984/11/13/005.

[7] A.Y. Didyk, et al., The behavior of amorphous alloys under swift heavy ion irradiation at room temperature, Nukleonika 50 (4) (2005) 149–152.

[8] M. Iqbal, A. Qayyum, J.I. Akhter, Surface modification of Zr-based bulk amorphous alloys by using ion irradiation, J. Alloy. Compd. 509 (6) (2011) 2780–2783, https://doi.org/10.1016/j.jallcom.2010.11.098.

[9] Y. Fukumoto et al., Behavior of Free Volume in Zrcual Bulk Metallic Glass after Irradiation, In: Journal of Physics: Conference Series, vol. 225, IOP Publishing, 2010.10.1088/1742-6596/225/1/012010.

[10] X. Bian, et al., Manipulation of free volumes in a metallic glass through xe-ion irradiation, Acta Mater. 106 (2016) 66–77, https://doi.org/10.1016/j.actamat.2016.01.002.

[11] J. Sun, et al., Study of local crystallization induced in FeSiNbZrB amorphous alloy by swift heavy ion (SHI) irradiation at room temperature, nuclear instruments and methods in physics research, Sect. B Beam Interact. Mater. At. 307 (2013) 486–490, https://doi.org/10.1016/j.nimb.2013.02.045.

[12] W.F. Cureton, C.L. Tracy, M. Lang, Review of swift heavy ion irradiation effects in ceo2, Quantum Beam Sci. 5 (2) (2021), https://doi.org/10.3390/qubs5020019.

[13] M. Toulemonde, C. Dufour, E. Paumier, Transient thermal process after a high-energy heavy-ion irradiation of amorphous metals and semiconductors, Phys. Rev. B 46 (22) (1992) 14362, https://doi.org/10.1016/S0168-583X(99)00799-5.

[14] H. Trinkaus, Local stress relaxation in thermal spikes as a possible cause for creep and macroscopic stress relaxation of amorphous solids under irradiation, J. Nucl. Mater. 223 (2) (1995) 196–201, https://doi.org/10.1016/0022-3115(95)00013-5.

[15] R. Fleischer, P. Price, R. Walker, Ion explosion spike mechanism for formation of charged-particle tracks in solids, J. Appl. Phys. 36 (11) (1965) 3645–3652, https://doi.org/10.13140/RG.2.1.3815.0640.

[16] G. Bonfiglioli, A. Ferro, A. Mojoni, Electron microscope investigation on the nature of tracks of fission products in mica, J. Appl. Phys. 32 (12) (1961) 2499–2503, https://doi.org/10.1063/1.1728339.

[17] M. Toulemonde, et al., Nanometric transformation of the matter by short and intense electronic excitation: Experimental data versus inelastic thermal spike model, Nucl. Instrum. Methods Phys. Res. Sect. B Beam Interact. Mater. At. 277 (2012) 28–39, https://doi.org/10.1016/j.nimb.2011.12.045.

[18] S. Klaumünzer, G. Schumacher, Dramatic growth of glassy Pd80Si20 during heavy-ion irradiation, Phys. Rev. Lett. 51 (21) (1983) 1987–1990, https://doi.org/10.1103/PhysRevLett.51.1987.

[19] W. Boukhemkhem, et al., Swift heavy ion irradiation effect on structural, morphological and mechanical properties of zr70ni30 metallic glass, Phys. Scr. 98 (8) (2023) 085311, https://doi.org/10.1088/1402-4896/ace387.

[20] C. Trautmann, S. Klaumünzer, H. Trinkaus, Effect of stress on track formation in amorphous iron boron alloy: ion tracks as elastic inclusions, Phys. Rev. Lett. 85 (17) (2000) 3648, https://doi.org/10.1103/PhysRevLett.85.3648.

[21] M.D. Rodríguez, et al., Morphology of swift heavy ion tracks in metallic glasses, J. Non-Cryst. Solids 358 (3) (2012) 571–576, https://doi.org/10.1016/j.jnoncrysol.2011.10.028.

[22] J. Sun, et al., Study of local crystallization induced in FeSiNbZrB amorphous alloy by swift heavy ion (SHI) irradiation at room temperature, nuclear instruments and methods in physics research, Sect. B Beam Interact. Mater. At. 307 (2013) 486–490, https://doi.org/10.1016/j.nimb.2013.02.045.

[23] H. Zhou, et al., X-ray photon correlation spectroscopy revealing the change of relaxation dynamics of a severely deformed Pd-based bulk metallic glass, Acta Mater. 195 (June) (2020) 446–453, https://doi.org/10.1016/j.actamat.2020.05.064.

[24] J.F. Ziegler, M.D. Ziegler, J.P. Biersack, SRIM - the stopping and range of ions in matter (2010), Nucl. Instrum. Methods Phys. Res. Sect. B Beam Interact. Mater. At. 268 (11-12) (2010) 1818–1823, https://doi.org/10.1016/j.nimb.2010.02.091.

[25] J.S. Hwang, K.J. Lin, C. Tien, Measurement of heat capacity by fitting the whole temperature response of a heat-pulse calorimeter, Rev. Sci. Instrum. 68 (1) (1997) 94–101, https://doi.org/10.1063/1.1147722.

[26] S. Wei, et al., Crystallization of amorphous Zr65Cu27Al8 alloy with wide supercooled liquid region, Mater. Lett. 37 (4-5) (1998) 263–267, https://doi.org/10.1016/S0167-577X(98)00103-7.

[27] D. Gärtner, et al., Techniques of tracer diffusion measurements in metals, alloys and compounds, Diffus. Found. 29 (2021) 31–73, https://doi.org/10.4028/www.scientific.net/DF.29.31.

[28] G.M. Pharr, J.H. Strader, W.C. Oliver, Critical issues in making small-depth mechanical property measurements by nanoindentation with continuous stiffness measurement, J. Mater. Res. 24 (3) (2009) 653–666, https://doi.org/10.1557/jmr.2009.0096.

[29] W.C. Oliver, G.M. Pharr, Measurement of hardness and elastic modulus by instrumented indentation: advances in understanding and refinements to methodology, J. Mater. Res. 19 (1) (2004) 3–20, https://doi.org/10.1557/jmr.2004.19.1.3.

[30] W.C. Oliver, G.M. Pharr, An improved technique for determining hardness and elastic madulus using load and displacement, J. Mater. Res. 7 (1) (1992) 1564–1583, https://doi.org/10.1557/JMR.1992.1564.

[31] N. Nollmann, et al., Impact of micro-alloying on the plasticity of Pd-based bulk metallic glasses, Scr. Mater. 111 (2016) 119–122, https://doi.org/10.1016/j.scriptamat.2015.08.030.

[32] S. Hilke, H. Rösner, G. Wilde, The role of minor alloying in the plasticity of bulk metallic glasses, Scr. Mater. 188 (2020) 50–53, https://doi.org/10.1016/j.scriptamat.2020.06.070.

[33] A. Hassanpour, et al., Impact of severe plastic deformation on the relaxation of glassy and supercooled liquid states of amorphous Pd40Ni40P20, J. Appl. Phys. 128 (15) (2020), https://doi.org/10.1063/5.0026950.

[34] J. Bünz, et al., Low temperature heat capacity of a severely deformed metallic glass, Phys. Rev. Lett. 112 (13) (2014), https://doi.org/10.1103/PhysRevLett.112.135501.

[35] T. Malis, S. Cheng, R. Egerton, EELS log-ratio technique for specimen-thickness measurement in the tem, J. Electron Microsc. Tech. 8 (2) (1988) 193–200, https://doi.org/10.1002/jemt.1060080206.

[36] T. Iwai, et al., Method for detecting subtle spatial structures by fluctuation microscopy, Phys. Rev. B 60 (1) (1999) 191, https://doi.org/10.1103/PhysRevB.60.191.

[37] P. Voyles, J. Gibson, M. Treacy, Fluctuation microscopy: a probe of atomic correlations in disordered materials, Microscopy 49 (2) (2000) 259–266, https://doi.org/10.1093/oxfordjournals.jmicro.a023805.

[38] P. Voyles, D. Muller, Fluctuation microscopy in the STEM, Ultramicroscopy 93 (2) (2002) 147–159, https://doi.org/10.1016/S0304-3991(02)00155-9.

[39] F. Yi, P. Voyles, Effect of sample thickness, energy filtering, and probe coherence on fluctuation electron microscopy experiments, Ultramicroscopy 111 (8) (2011) 1375–1380, https://doi.org/10.1016/j.ultramic.2011.05.004.

[40] J. Hwang, P. Voyles, Variable resolution fluctuation electron microscopy on Cu-Zr metallic glass using a wide range of coherent STEM probe size, Microsc. Microanal. 17 (1) (2011) 67–74, https://doi.org/10.1017/S1431927610094109.

[41] M. Treacy, J. Gibson, Variable coherence microscopy: a rich source of structural information from disordered materials, Acta Crystallogr. Sect. A Found. Crystallogr. 52 (2) (1996) 212–220, https://doi.org/10.1107/S0108767395012876.

[42] M. Treacy, et al., Fluctuation microscopy: a probe of medium range order, Rep. Prog. Phys. 68 (12) (2005) 2899, https://doi.org/10.1088/0034-4885/68/12/R06.

[43] F. Yi, P. Tiemeijer, P.M. Voyles, Flexible formation of coherent probes on an aberration-corrected STEM with three condensers, J. Electron Microsc. 59 (S1) (2010) S15–S21, https://doi.org/10.1093/jmicro/dfq052.

[44] M. Treacy, When structural noise is the signal: speckle statistics in fluctuation electron microscopy, Ultramicroscopy 107 (2-3) (2007) 166–171, https://doi.org/10.1016/j.ultramic.2006.07.001.

[45] M. Treacy, et al., Probing medium-range structural correlations by fluctuation microscopy, J. Phys. Condens. Matter 19 (45) (2007) 455201, https://doi.org/10.1088/09538984/19/45/455201.

[46] F.A. Davani, et al., Correlations between the ductility and medium-range order of bulk metallic glasses, J. Appl. Phys. 128 (1) (2020) 015103, https://doi.org/10.1063/5.0007564.

[47] W. Stratton, P. Voyles, A phenomenological model of fluctuation electron microscopy for a nanocrystal/amorphous composite, Ultramicroscopy 108 (2008) 727–736, https://doi.org/10.1016/j.ultramic.2007.11.004.

[48] B. Kestel, Non-acid electrolyte thins many materials for TEM without causing hydride formation, Ultramicroscopy 19 (2) (1986) 205–211, https://doi.org/10.1016/0304-3991(86)90208-1.

[49] G. Rizza, From ion-hammering to ion-shaping: an historical overview, J. Phys. Conf. Ser. 629 (1) (2015) 012005, https://doi.org/10.1088/1742-6596/629/1/012005.

[50] A. Gutzmann, S. Klaumünzer, Shape instability of amorphous materials during high-energy ion bombardment, nuclear instruments and methods in physics research, Sect. B Beam Interact. Mater. At. 127-128 (1997) 12–17, https://doi.org/10.1016/S0168-583X(96)00841-5.

[51] H. Narayan, et al., Surface smoothing of metallic glasses by swift heavy ion irradiation, nuclear instruments and methods in physics research, Sect. B Beam Interact. Mater. At. 156 (1) (1999) 217–221, https://doi.org/10.1016/S0168583X(99)00265-7.

[52] P. Tuinstra, et al., The calorimetric glass transition of amorphous Pd40 Ni40 P20, Acta Metall. Et. Mater. 43 (7) (1995) 2815–2823, https://doi.org/10.1016/09567151(94)00450-V.

[53] I.R. Lu, et al., Thermodynamic properties of Pd-based glass-forming alloys, J. Non-Cryst. Solids 250-252 (1999) 577–581, https://doi.org/10.1016/S0022-3093(99)00135-0. ⟨www.elsevier.com/locate/jnoncrysol⟩.

[54] J.C. Qiao, J.M. Pelletier, Isochronal and isothermal crystallization in Zr 55Cu 30Ni 5 Al 10 bulk metallic glass, Trans. Nonferrous Met. Soc. China 22 (3) (2012) 577–584, https://doi.org/10.1016/S1003-6326(11)61216-8.

[55] Y.H. Liu, et al., Super plastic bulk metallic glasses at room temperature, Science 315 (5817) (2007) 1385–1388, https://doi.org/10.1126/science.1136726.

[56] D. Turnbull, M.H. Cohen, Free-volume model of the amorphous phase: glass transition, J. Chem. Phys. 34 (1) (1961) 120–125, https://doi.org/10.1063/1.1731549.

[57] E.C. Tool A.Q, Variations caused in the heating curves of glass by heat treatment - I. Introduction In a previous articlea attention was called to the fact that the form of the, J. Am. Ceram. Soc. 14 (1931) 276–308, j.11512916.1931.tb16602.x.

[58] H. Zhou, et al., Two-stage rejuvenation and the correlation between rejuvenation behavior and the boson heat capacity peak of a bulk metallic glass, Acta Mater. 179 (2019) 308–316, https://doi.org/10.1016/j.actamat.2019.08.040.

[59] M. Wakeda, et al., Controlled rejuvenation of amorphous metals with thermal processing, Sci. Rep. 5 (2015), https://doi.org/10.1038/srep10545.

[60] Y. Sun, A. Concustell, A.L. Greer, Thermomechanical processing of metallic glasses: extending the range of the glassy state, Nat. Rev. Mater. 1 (9) (2016) 1–14, https://doi.org/10.1088/2752-5724/ac4558.

[61] A. Hassanpour, et al., Impact of severe plastic deformation on the relaxation of glassy and supercooled liquid states of amorphous Pd40Ni40P20, J. Appl. Phys. 128 (15) (2020), https://doi.org/10.1063/5.0026950.

[62] Y.P. Mitrofanov, et al., Impact of plastic deformation and shear band formation on the boson heat capacity peak of a bulk metallic glass, Phys. Rev. Lett. 112 (13) (2014), https://doi.org/10.1103/PhysRevLett.112.135901.

[63] H. Shintani, H. Tanaka, Universal link between the boson peak and transverse phonons in glass, Nat. Mater. 7 (11) (2008) 870–877, https://doi.org/10.1038/nmat2293.

[64] P.A. Duine, J. Sietsma, A. Van Den Beukel, Atomic transport in amorphous Pd40Ni40P20 near the glass-transition temperature: Au diffusivity and viscosity, Phys. Rev. B 48 (10) (1993) 6957–6965, https://doi.org/10.1103/PhysRevB.48.6957.

[65] K. Knorr, et al., Self-diffusion in the amorphous and supercooled liquid state of the bulk metallic glass Zr46.75Ti8.25Cu7.5Ni10Be27.5, J. Non-Cryst. Solids 250-252 (1999) 669–673, https://doi.org/10.1016/S0022-3093(99)00157-X.

[66] D.M. Herlach, Non-equilibrium solidification of undercooled metallic metls, Mater. Sci. Eng. R Rep. 12 (4-5) (1994) 177–272, https://doi.org/10.1016/0927796X(94)90011-6.

[67] P. Duine, J. Sietsma, A. Van den Beukel, Defects in amorphous PdNiP and their role in the diffusion process. Defect and Diffusion forum, Trans Tech Publ., 1995, pp. 91–110, https://doi.org/10.4028/www.scientific.net/DDF.117-118.91. Vol. 117.

[68] A. Van den Beukel, On the parameters governing atomic mobility in metallic glasses, Phys. Status Solidi (a) 128 (2) (1991) 285–293, https://doi.org/10.1002/pssa.2211280203.

[69] S. Sharma, F. Faupel, Correlation between effective activation energy and pre-exponential factor for diffusion in bulk metallic glasses, J. Mater. Res. 14 (1999) 3200–3203, https://doi.org/10.1557/JMR.1999.0431.

[70] A. Paul, et al., Thermodynamics, Diffusion and the Kirkendall Effect in Solids, Springer, 2014, https://doi.org/10.1007/978-3-319-07461-0.

[71] S. Michalik, et al., The effects of swift Xe ion bombardment on the amorphous structure of a Vitroperm type alloy, J. Alloy. Compd. 795 (2019) 69–78, https://doi.org/10.1016/j.jallcom.2019.04.328.

[72] H.S. Chen, J.T. Krause, E. Coleman, Elastic constants, hardness and their implications to flow properties of metallic glasses, J. Non-Cryst. Solids 18 (2) (1975) 157–171, https://doi.org/10.1016/0022-3093(75)90018-6.

[73] A.S. Argon, H.Y. Kuo, Plastic flow in a disordered bubble raft (an analog of a metallic glass), Mater. Sci. Eng. 39 (1) (1979) 101–109, https://doi.org/10.1016/0025-5416(79)90174-5.

[74] A.S. Argon, L.T. Shi, Development of visco-plastic deformation in metallic glasses, Acta Metall. 31 (4) (1983) 499–507, https://doi.org/10.1016/0001-6160(83)90038-X.

[75] C.A. Schuh, Nanoindentation studies of materials, Mater. Today 9 (5) (2006) 32–40, https://doi.org/10.1016/S1369-7021(06)71495-X.

[76] I.C. Choi, et al., Estimation of the shear transformation zone size in a bulk metallic glass through statistical analysis of the first pop-in stresses during spherical nanoindentation, Scr. Mater. 66 (11) (2012) 923–926, https://doi.org/10.1016/j.scriptamat.2012.02.032.

[77] J. Musil, et al., Relationships between hardness, Young's modulus and elastic recovery in hard nanocomposite coatings, Surf. Coat. Technol. 154 (2-3) (2002) 304–313, https://doi.org/10.1016/S0257-8972(01)01714-5.

[78] A. Leyland, A. Matthews, On the significance of the H/E ratio in wear control: a nanocomposite coating approach to optimised tribological behaviour, Wear 246 (1-2) (2000) 1–11, https://doi.org/10.1016/S0043-1648(00)00488-9.

[79] F. Spaepen, A microscopic mechanism for steady state inhomogeneous flow in metallic glasses, Acta Metall. 25 (4) (1977) 407–415, https://doi.org/10.1016/0001-6160(77)90232-2.

[80] H. Bei, S. Xie, E.P. George, Softening caused by profuse shear banding in a bulk metallic glass, Phys. Rev. Lett. 96 (10) (2006) 1–4, https://doi.org/10.1103/PhysRevLett.96.105503.

[81] L. Wang, et al., Effect of residual stresses on the hardness of bulk metallic glasses, Acta Mater. 59 (7) (2011) 2858–2864, https://doi.org/10.1016/j.actamat.2011.01.025.

[82] G. Rizza, A. Dunlop, M. Kopcewicz, Deformation bands in metallic glasses induced by swift heavy ions, Nucl. Instrum. Methods Phys. Res. Sect. B Beam Interact. Mater. At. 245 (1) (2006) 130–132, https://doi.org/10.1016/J.NIMB.2005.11.089.

[83] D. Şopu, et al., Atomic-scale origin of shear band multiplication in heterogeneous metallic glasses, Scr. Mater. 178 (2020) 57–61, https://doi.org/10.1016/j.scriptamat.2019.11.006.

[84] D. Şopu, et al., Structure-property relationships in nanoporous metallic glasses, Acta Mater. 106 (2016) 199–207, https://doi.org/10.1016/j.actamat.2015.12.026.

[85] C. Hubert, et al., Swift heavy ion-induced radiation damage in isotropic graphite studied by micro-indentation and in-situ electrical resistivity, Nucl. Instrum. Methods Phys. Res. Sect. B Beam Interact. Mater. At. 365 (2015) 509–514, https://doi.org/10.1016/j.nimb.2015.08.056.

[86] I. Manika, et al., Nanoindentation and raman spectroscopic study of graphite irradiated with swift 238u ions, Fuller. Nanotub. Carbon Nanostruct. 20 (4-7) (2012) 548–552, https://doi.org/10.1080/1536383X.2012.656064.

[87] I. Manika, et al., Energy loss and fluence dependency of swift-ion-induced hardening in LiF, Phys. Status Solidi C. 2 (1) (2005) 434–437, https://doi.org/10.1016/j.nimb.2005.11.113.

[88] S. Hilke, et al., The influence of deformation on the medium-range order of a Zr-based bulk metallic glass characterized by variable resolution fluctuation electron microscopy, Acta Mater. 171 (2019) 275–281, https://doi.org/10.1016/j.actamat.2019.04.

[89] S. Hilke, H. Rösner, G. Wilde, The role of minor alloying in the plasticity of bulk metallic glasses, Scr. Mater. 188 (2020) 50–53, https://doi.org/10.1016/j.scriptamat.2020.06.070.

[90] M. Stringe, H. Rösner, G. Wilde, Evidence for strain and a structural reset in Pd40Ni40P20bulk metallic glass, J. Appl. Phys. 132 (10) (2022), https://doi.org/10.1063/5.0098050.

[91] S.N. Bogle, et al., Quantifying nanoscale order in amorphous materials: simulating fluctuation electron microscopy of amorphous silicon, J. Phys. Condens. Matter 19 (45) (2007) 455204, https://doi.org/10.1088/0953-8984/19/45/455204.

[92] S.N. Bogle, et al., Size analysis of nanoscale order in amorphous materials by variable-resolution fluctuation electron microscopy, Ultramicroscopy 110 (10) (2010) 1273–1278.

[93] J. Gibson, et al., Substantial crystalline topology in amorphous silicon, Phys. Rev. Lett. 105 (12) (2010) 125504, https://doi.org/10.1103/PhysRevLett.105.125504.

[94] M. Stringe, et al., Decoupled alpha and beta relaxation kinetics in a thermally cycled bulk Pd40Ni40P20 glass, J. Alloy. Compd. 915 (2022) 165386, https://doi.org/10.1016/j.jallcom.2022.165386.

[95] T. Nagase, et al., MeV electron irradiation induced crystallization in metallic glasses: atomic structure, crystallization mechanism and stability of an amorphous phase under the irradiation, J. Non-Cryst. Solids 358 (3) (2012) 502–518, https://doi.org/10.1016/j.jnoncrysol.2011.11.010.

[96] M.H. Cohen, G.S. Grest, Liquid-glass transition, a free-volume approach, Phys. Rev. B 20 (3) (1979) 1077–1098, https://doi.org/10.1103/PhysRevB.20.1077.

[97] M.H. Cohen, D. Turnbull, Molecular transport in liquids and glasses, J. Chem. Phys. 31 (5) (1959) 1164–1169, https://doi.org/10.1063/1.1730566.

[98] J.F. Gibbons, Ion implantation in semiconductors—part II: damage production and annealing, Proc. IEEE 60 (9) (1972) 1062–1096, https://doi.org/10.1109/PROC.1972.8854.

[99] W. Weber, Models and mechanisms of irradiation-induced amorphization in ceramics, Nucl. Instrum. Methods Phys. Res. Sect. B Beam Interact. Mater. At. 166 (2000) 98–106, https://doi.org/10.1016/S0168-583X(99)00643-6.

[100] A. Meftah, et al., Experimental determination of track cross-section in gd3ga5o12 and comparison to the inelastic thermal spike model applied to several materials, Nucl. Instrum. Methods Phys. Res. Sect. B Beam Interact. Mater. At. 237 (3-4) (2005) 563–574, https://doi.org/10.1016/j.nimb.2005.02.025.

[101] A. Kamarou, et al., Radiation damage formation in InP, InSb, GaAs, GaP, Ge, and Si due to fast ions, Phys. Rev. B 78 (5) (2008) 054111, https://doi.org/10.1103/PhysRevB.78.054111.

[102] Z. Wang, et al., The se sensitivity of metals under swift-heavy-ion irradiation: a transient thermal process, J. Phys. Condens. Matter 6 (34) (1994) 6733, https://doi.org/10.1088/0953-8984/6/34/006.

[103] M. Toulemonde, et al., Track formation and fabrication of nanostructures with MeV-ion beams, Nucl. Instrum. Methods Phys. Res. Sect. B Beam Interact. Mater. At. 216 (2004) 1–8, https://doi.org/10.1016/j.nimb.2003.11.013.

[104] A. Kaiser, Electron-phonon enhancement of thermopower: application to metallic glasses, Phys. Rev. B 29 (12) (1984) 7088, https://doi.org/10.1103/PhysRevB.29.7088.

[105] S. Poon, K. Wong, A. Drehman, Localization and electron-interaction effects in metallic glasses, Phys. Rev. B 31 (3) (1985) 1668, https://doi.org/10.1103/PhysRevB.31.1668.

[106] B. Gallagher, B. Hickey, The thermopower of metallic glasses, J. Phys. F Met. Phys. 15 (4) (1985) 911, https://doi.org/10.1088/0305-4608/15/4/015.

[107] S.V. Ketov, et al., Rejuvenation of metallic glasses by non-affine thermal strain, Nature 524 (7564) (2015) 200–203, https://doi.org/10.1038/nature14674.

[108] M. Bruns, et al., Decelerated aging in metallic glasses by low temperature thermal cycling, Phys. Rev. Res. 3 (1) (2021) 013234, https://doi.org/10.1103/PhysRevResearch.3013234.